Title	Development of bifunctional oriented bioactive glass/poly(lactic acid) composite scaffolds to control osteoblast alignment and proliferation
Author(s)	Lee, Sungho; Matsugaki, Aira; Kasuga, Toshihiro et al.
Citation	Journal of Biomedical Materials Research - Part A. 107(5) p.1031-p.1041
Issue Date	2019-01-24
oaire:version	VoR
URL	https://hdl.handle.net/11094/89821
rights	This article is licensed under a Creative Commons Attribution-NonCommercial 4.0 International License.
Note	

Development of bifunctional oriented bioactive glass/poly(lactic acid) composite scaffolds to control osteoblast alignment and proliferation

Sungho Lee,[1] Aira Matsugaki,[1] Toshihiro Kasuga,[2] Takayoshi Nakano[1]

[1]Division of Materials and Manufacturing Science, Graduate School of Engineering, Osaka University, Osaka, Japan
[2]Division of Advanced Ceramics, Graduate School of Engineering, Nagoya Institute of Technology, Nagoya, Japan

Abstract: During the bone regeneration process, the anisotropic microstructure of bone tissue (bone quality) recovers much later than bone mass (bone quantity), resulting in severe mechanical dysfunction in the bone. Hence, restoration of bone microstructure in parallel with bone mass is necessary for ideal bone tissue regeneration; for this, development of advanced bifunctional biomaterials, which control both the quality and quantity in regenerated bone, is required. We developed novel oriented bioactive glass/poly(lactic acid) composite scaffolds by introducing an effective methodology for controlling cell alignment and proliferation, which play important roles for achieving bone anisotropy and bone mass, respectively. Our strategy is to manipulate the cell alignment and proliferation by the morphological control of the scaffolds in combination with controlled ion release from bioactive glasses. We quantitatively controlled the morphology of fibermats containing bioactive glasses by electrospinning, which successfully induced cell alignment along the fibermats. Also, the substitution of CaO in Bioglass®(45S5) with MgO and SrO improved osteoblast proliferation, indicating that dissolved Mg^{2+} and Sr^{2+} ions promoted cell adhesion and proliferation. Our results indicate that the fibermats developed in this work are candidates for the scaffolds to bone tissue regeneration that enable recovery of both bone quality and bone quantity. © 2019 The Authors. *journal Of Biomedical Materials Research Part A* Published By Wiley Periodicals, Inc. J Biomed Mater Res Part A: 107A: 1031–1041, 2019.

Key Words: biomaterial, bioactive glass, bone anisotropy, electrospinning, bone quality

INTRODUCTION

Bone is a highly calcified tissue consisting of collagen fibrils and biological apatite (BAp) with several hierarchical levels from nano to microscale.[1] Importantly, the multiscale structure of bone tissue exhibits highly anisotropic properties associated with collagen fibril orientation and the direction of the *c*-axis of BAp crystals.[2,3] The anisotropic microstructure of bone tissue is one of the most important "bone quality" indices, which mainly governs the mechanical performance of bone tissue rather than bone mass ("bone quantity").[4] During the bone regeneration process, the recovery of anisotropic bone microstructure is significantly delayed compared to the bone mineral density (BMD) restoration, which induces severe mechanical dysfunction.[4] The development of bifunctional biomaterials with controllable "bone quality" and "bone quantity" is therefore necessary for the recovery of highly ordered healthy bone tissue. Control of cell alignment is a valuable strategy for constructing anisotropic bone matrices; collagen/apatite matrix alignment depends on the osteoblast orientation.[5] Moreover, the degree of BAp *c*-axis orientation shows a dependence on the directional distribution of osteoblasts.[6] Accordingly, directional and quantitative control of osteoblasts can be determinative for achieving satisfactory bone tissue with both "quality" and "quantity."

Bioglass® introduced the concept of bioactive materials; chemical cues from the material indicate enhanced metabolism and accelerated healing of damaged bone.[7,8] Xynos *et al*. reported that the dissolved silicate, calcium, and orthophosphate ions from Bioglass® stimulated human osteoblast proliferation by increasing the production of insulin-like growth factor II (IGF-II).[9–11] Magnesium ions promote cell adhesion, proliferation, differentiation, and subsequent mineralization.[12–15] The expression of various integrin family members, which are a class of adhesion proteins, was increased by Mg^{2+} ions.[13] Strontium ions have several effects on the stimulation of osteoblast proliferation and differentiation and the inhibition of

preosteoclast differentiation.[16–18] Sr^{2+} ions increase the mRNA levels of c-fos and egr-1, which are involved in cell proliferation.[16] They also promote the metabolism of osteoblasts due to activation of calcium-sensing receptors,[16,19] and increase alkaline phosphatase (ALP) activity,[20] which is a marker for osteoblast differentiation. Osteoprotegerin (OPG) was upregulated by Sr^{2+} ions and accompanied the downregulation of receptor activators of nuclear factor kappa B (RANK) ligand expression, which involve differentiation of pre-osteoclasts.[18]

Electrospinning is a useful method for fabricating fibrous scaffolds, which can be applied to biomimetic templates for cell adhesion, proliferation, differentiation, and mineralization of damaged tissue. Obata et al. reported the use of poly (L-lactic acid) (PLLA) micro-fibermats containing silicon-doped vaterite for guided bone regeneration (GBR) membranes.[21] Proliferation of osteoblasts on the fibermats was improved by dissolved silicate ions. In vivo, newly formed bone was observed over 4 weeks, and the defect was covered after 12 weeks. Fibroblasts (NIH3T3) on the oriented nanofiber scaffold were elongate and aligned parallel to the fibers, and their gene expression upregulated associated with actin production, action polymerization, and focal adhesion formation than random one.[22] Human mesenchymal stem cells (hMSC) on PLLA aligned nano-fibermats were highly oriented in the direction of the collector, where the cells were stretched along the long axis of the nanofibers.[23,24] Subsequently, the collagen fibril bundles produced by hMSC were aligned in the direction of the cell adhesion (i.e., the nano-fiber direction). Tujunen et al.[25] reported that mouse osteoblast-like cells on PLLA/siloxane-doped vaterite aligned micro-fibermats were oriented in the fiber orientation direction and elongated along the microfiber.

The aim of this study is to create a novel bifunctional biomaterial for bone tissue regeneration, which achieve recovery of both bone quality (oriented bone microstructure) and bone quantity (bone mass). The oriented fibermats were prepared with bioactive glass/PLLA composites by electrospinning an anisotropic scaffold to control cell alignment. PLLA, which is the most widely used biodegradable polymer in the biomaterials field, was chosen for fabrication of the oriented fibermat. The glasses in the composites were prepared by substituting the CaO in Bioglass® (45S5) with MgO and SrO to improve bone regeneration with the dissolved ions from the glasses. Herein, a fundamental investigation on the design of oriented bioactive glass/PLLA fibermats for biomedical applications is reported, evaluating their anisotropic morphology, ion-releasing ability, and cell behavior on the fibermats.

MATERIALS AND METHODS
Preparation of the bioactive glasses
Glasses with compositions of $46.1SiO_2 \cdot 24.4Na_2O \cdot 26.9MO \cdot 2.6P_2O_5$ (mol%, M = Ca, Mg, or Sr, denoted by BG_M) were prepared by melt quenching. Glass batches were prepared by mixing SiO_2 (99.0%), Na_2CO_3 (99.5%), $CaCO_3$ (99.5%), MgO (99.0%), $SrCO_3$ (98.0%), and NaH_2PO_4 (99.0%). All the reagents were purchased from Kishida Chemical Co. The batches were melted in a platinum crucible at 1500°C for 30 min and quenched by

pressing with two stainless steel plates. The glasses were examined using laser Raman spectroscopy in between 220 and 1300 cm^{-1} (NRS-5100, JASCO). The resulting glasses were pulverized using an automatic alumina mortar, and the powders were stored in a desiccator. The resulting powders were observed by field emission gun electron microscopy (SEM, JSM-6500, JEOL) with an accelerating voltage of 15 kV after coating the samples with an amorphous osmium layer using an osmium coater (Neoc CS, Meiwafosis Co. Ltd.). Particles diameter were measured using the ImageJ software (NIH).

Preparation of the composite pellets
BG_M powders were mixed with PLLA (LACEA, molecular weight of 140 kDa, Mitsui Chemical) by a melt-blending method using a kneader (PBV-0.1, Irie Shokai) at 190°C for 10 min, resulting in BG_M/PLLA composite pellets. The volume ratios of BG_M powders in the composites were set to 10 and 30 vol.%. The volumes of PLLA and BG_M powders were calculated from their density. The densities were measured by an Archimedes' method using acetone and water as immersion fluid for BG_M and PLLA, respectively, at 25°C (n = 3). Molecular weight distributions of the composites were determined by gel permeation chromatography (GPC, Prominence, Shimadzu) using a KF-806L column (Shodex). For detection, a Shimadzu refractometer RID-10A was used. Chloroform (99.7%, HPLC grade, Wako Pure Chemical) was used as the eluent flowing at 1 mL·min^{-1} at 35°C. The composites were manually injected (20 μL) at a concentration varying between 10 and 15 mg·mL^{-1}. Average molecular weights and distributions were determined against a linear polystyrene calibrant.

Preparation of the oriented fibermats
The oriented fibermats with the composites were prepared by an electrospinning method, and that with PLLA was prepared as a control for cell proliferation test. The composite pellets and PLLA were dissolved in chloroform (99.0%, Wako Pure Chemical) at 14 wt.% PLLA to prepare the solution for electrospinning. In our preliminary experiments, this ratio was found to be optimal for preparing the oriented fibermats. In case of 10 vol.% BG_{Mg} composite, the pellet was dissolved in chloroform at 10 wt.% PLLA, since the 14 wt.% solution could not be ejected from the syringe. The viscosities of the prepared solutions were measured using a vibration-type viscometer (VM-10A-M, Sekonic Co.). Subsequently, the prepared solutions were loaded into a syringe pump (FP-1100, Melquest, Japan) with an 18 gauge syringe needle, which was set at a discharge rate of 0.15 mL·min^{-1}. A high-voltage supply (HARb-40P0.75, Matsusada Precision Inc.) was used to apply voltages of 16 kV at the needle tip. The distance between the needle tip and the drum collector was maintained at 200 mm. The drum collector (diameter 30 mm) was rotated at 3000 rpm (4.7 m·s^{-1}). The obtained fibermats were denoted by BG_Mx, where BG_M is sample code for the bioactive glass and x (x = 10 or 30) is the vol.% of BG_M in the composite. The electrospinning was carried out at room temperature (approximately 25°C) and approximately 40% relative humidity.

Morphology of the fibermats

The morphology of the prepared fibermats was observed by SEM with an accelerating voltage of 3 kV after coating the samples with an amorphous osmium layer using an osmium coater. Fiber diameter and the angle (θ) between the fiber and collector rotation direction were measured using the ImageJ software (NIH).

Ion-releasing behavior of the fibermats

To characterize the ion-releasing behavior from the fibermats, samples of 14 mm diameter and 120–160 μm thickness were soaked in 10 mL of 50 mM Tris buffer solution (TBS, pH 7.40, 37°C) for 9 days. The concentrations of Si, P, Ca^{2+}, Mg^{2+}, and Sr^{2+} ions in the TBS were measured by inductively coupled plasma optical emission spectroscopy (ICP-OES, Agilent 720 ICP, Agilent Technologies). The fraction of weight released of various elements in TBS were calculated as follows;

$$\text{Release percentage } (\%) = \frac{a \times V_{\text{solution}}}{M_{\text{sample}} \times W_{\text{glass}} \times Frac_{,a}} \qquad (1)$$

where a is the concentration of the element of interest in $mg \cdot L^{-1}$, V_{solution} is the volume of soaked solution in L, $Frac_{,a}$ is the nominal weight fraction of the element in the glass, M_{sample} is weight of the sample in mg, and W_{glass} is the wt.% of the glass in the fibermat. After soaking in TBS for 9 days, the fibermats were analyzed by X-ray diffractometry (XRD, X'pert PRO, Phillips) using Cu Kα radiation.

Osteoblast proliferation on the fibermats

Fibermats with 8 mm diameter were prepared for osteoblast tests. A PLLA oriented fibermat was used for the control. The samples were soaked in 70% ethanol for 30 s and subsequently dried under ultra violet (UV) light for 30 min for sterilization. The cells were cultured in alpha-minimum essential medium (α-MEM, with L-glutamine and phenol red, Invitrogen) containing 10% fetal bovine serum (FBS, Invitrogen). The samples were placed into 48 well plates ($n = 4$), and mouse osteoblast-like cells (MC3T3-E1 cells) were seeded by adding 0.5 mL of the culture medium containing cells at a concentration of 3×10^4 cells·mL^{-1}. The culture medium was replaced after 1 day of culturing. After 1 and 3 days of culturing, the samples were washed with phosphate buffered saline (PBS), and 0.5 mL of α-MEM (no phenol red) and 50 μL of Cell Count Reagent SF (Nacalai Tesque) were added to the samples. After 2 h of incubation (37°C, 5% CO_2), the absorbance at 450 nm was evaluated using a microplate reader (Multiskan FC, Thermo Scientific). The number of cells was calculated by a standard curve between the number of cells and the absorbance of the resulting medium.

Primary osteoblast isolation and culture on the fibermats

Primary osteoblasts were isolated from newborn mouse calvariae as described in our previous report.[26] Briefly, calvariae from newborn C57BL/6 mice were excised under aseptic conditions, placed in ice-cold α-MEM, and then the fibrous tissues around the bone were gently removed. The calvariae were then subjected to a series of collagenase (Wako Pure Chemical)/trypsin (Nacalai Tesque) digestions at 37°C for 15 min each. The first two digests were discarded, since fibroblasts were mixed.[27] The supernatants of digests 3–5 were neutralized with α-MEM and pooled. The pooled solutions were filtered using a 100 μm mesh. The filtrates were centrifuged, and the resulting pellets were resuspended in α-MEM containing 10% FBS. The population of obtained cells was verified by real-time reverse transcription polymerase chain reaction (RT-PCR, Step-one, Applied Biosystems). The positive expression of typical osteoblast markers, collagen type I, ALP, and bone sialoprotein were confirmed, indicating the successful isolation of osteoblastic cell population in the present method. Fibermats with 14 mm diameter were prepared. The samples were soaked in 70% ethanol for 30 s and subsequently dried under UV light for 30 min for sterilization. The samples were placed into 24 well plates ($n = 4$), and primary osteoblast cells were seeded by adding 1.0 mL of the culture medium containing cells at a concentration of 3×10^4 cells·mL^{-1}. The culture medium was replaced after 1 day.

Fluorescence imaging of primary osteoblast

Primary osteoblasts were cultivated for 3 days on the samples, and the cells were fixed with 4% formaldehyde in PBS for 20 min. After washing three times with PBS-0.05% Triton X-100 (PBST), the cells were incubated in PBST containing 1% normal goat serum (NGS) for 30 min to block nonspecific antibody binding sites. Subsequently, the cells were incubated with mouse monoclonal antibodies against vinculin (Sigma-Aldrich) at 4°C for 12 h. The cells were incubated with Alexa Fluor® 546-conjugated anti-mouse IgG (Invitrogen) and Alexa Fluor® 488-conjugated phalloidin (Invitrogen). Finally, the cells were washed and mounted in Fluoro-KEEPER Antifade Reagent with DAPI (Nacalai Tesque). Fluorescent images were taken using a fluorescence microscope (BZ-X700, Keyence). The cell orientation angle (θ) against the collector rotation direction was analyzed using the Cell Profiler software (Broad Institute Cambridge).

Quantitative analysis for the degree of fiber and cell orientation

To evaluate the degrees of fiber and cell arrangement, the orientation order parameters FD and CD were calculated, where FD and CD are the degrees of fiber and cell alignment, respectively.[28] This system was derived using a distribution function $n(\theta)$, which is defined as the number of measured fibers or cells at the angle θ. The expected value of the mean square cosine $<cos^2\theta>$, FD, and CD were calculated as follows;

$$< cos^2 \theta > = \frac{\int_0^{2\pi} cos^2 \theta \cdot n(\theta) \, d\theta}{\int_0^{2\pi} n(\theta) \, d\theta} \qquad (2)$$

$$FD \text{ or } CD = 2 \left(< cos^2 \theta > - 0.5 \right) \qquad (3)$$

FD and CD take values ranging from −1 (fiber or cell completely aligned perpendicularly to the collector rotation
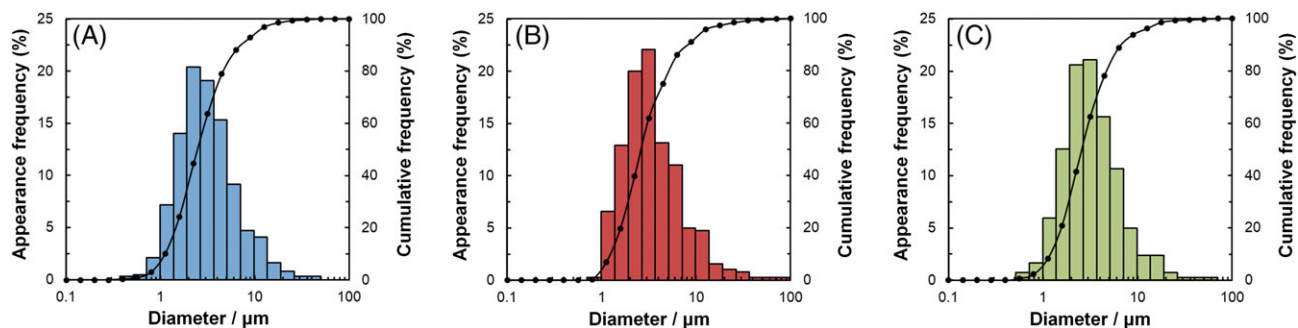
FIGURE 1. Powder diameter distribution of (A) BG_{Mg}, (B) BG_{Ca}, and (C) BG_{Sr}. Bar graphs represent appearance frequency and solid line represent cumulative frequency.

direction), to 0 (fiber or cell oriented randomly), to 1 (fiber or cell completely aligned parallel to the collector rotation direction).

Statistical analysis

Statistical significance was assessed by one-way ANOVA, followed by Tukey's post hoc test. A significance of $p < 0.05$ was required for rejection of the null hypothesis.

RESULTS
Glass and composite characterization

Densities of BG_{Mg}, BG_{Ca}, BG_{Sr}, and PLLA were 2.59, 2.72, 3.04, and 1.25 g/cm^3, respectively. Pulverized BG_{Mg}, BG_{Ca},

and BG_{Sr} diameters were approximately 2.7, 3.0, and 2.8 μm, respectively, and their distribution were shown in Figure 1. The particle diameter distribution between BG_M showed no significant difference. Laser Raman spectra of BG_M are shown in Figure 2A. The following Raman bands corresponding to the silicate Q_{Si}^n (n = 0–3) groups[29,30] and orthophosphate (Q_P^0) group[31,32] were observed: the symmetric stretching mode of Q_{Si}^3 (~1030 cm^{-1}), symmetric stretching mode of Q_{Si}^2 (~970 cm^{-1}), symmetric stretching mode of Q_{Si}^1 (~910 cm^{-1}), symmetric stretching mode of Q_{Si}^0 (~850 cm^{-1}), Si-O stretching linkages (~640 cm^{-1}), and symmetric stretching mode of the non-bridging oxygen in Q_P^0 (~950 cm^{-1}). BG_{Mg} may contain low amount of Q_{Si}^4
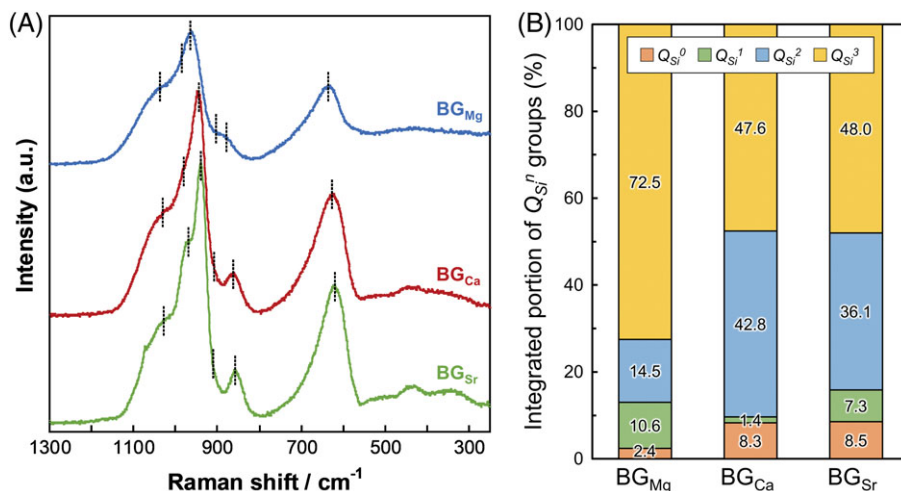

FIGURE 2. (A) Raman spectra for BG_M and (B) integrated portion of the Q_{Si}^n groups in BG_M.

TABLE I. Molecular Weights and Polydispersity Indices (M_w/M_n) of BG_M/PLLA Composites with 10 or 30 vol.% of BG_M and Viscosities of their Solutions with 14 wt.% of PLLA in Chloroform

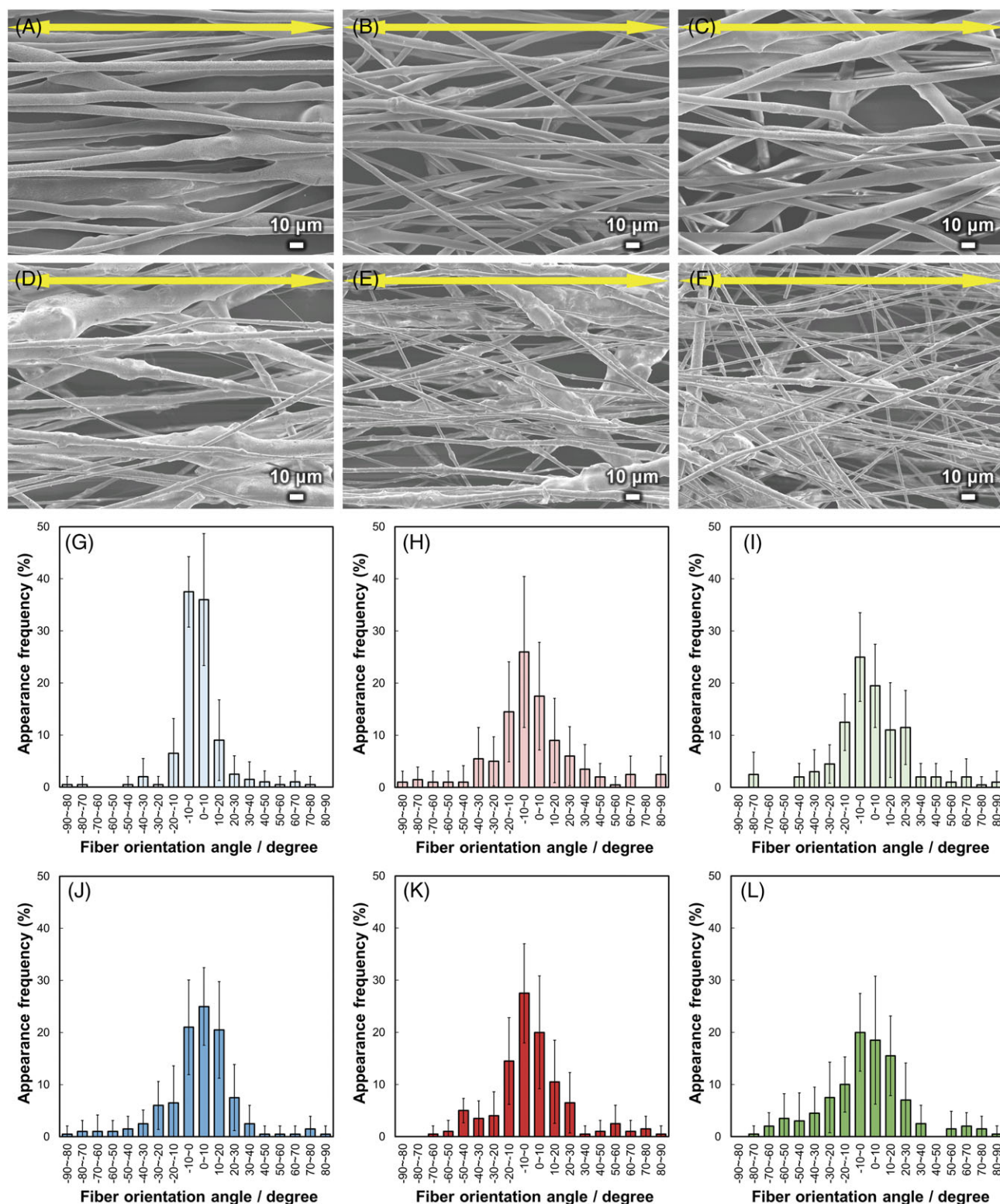| Samples		M_n/kDa	M_w/kDa	M_w/M_n	Viscosity/Pa·s
PLLA		51.4	94.9	1.8	1.3
BG_{Mg}	10 vol%	31.7	57.8	1.8	3.7
	30 vol%	23.0	54.8	2.4	2.3
BG_{Ca}	10 vol%	20.0	32.9	1.6	1.4
	30 vol%	15.9	41.0	2.6	1.3
BG_{Sr}	10 vol%	26.4	52.3	2.0	2.0
	30 vol%	19.0	47.1	2.5	1.2

FIGURE 3. SEM images of (A) $BG_{Mg}10$, (B) $BG_{Ca}10$, (C) $BG_{Sr}10$, (D) $BG_{Mg}30$, (E) $BG_{Ca}30$, and (F) $BG_{Sr}30$. Arrows indicate the collector rotation direction. Fiber orientation angle histograms for (G) $BG_{Mg}10$, (H) $BG_{Ca}10$, (I) $BG_{Sr}10$, (J) $BG_{Mg}30$, (K) $BG_{Ca}30$, and (L) $BG_{Sr}30$. Error bars represent the standard deviation.

(< 2%), which simulated by molecular dynamics.[33] However, the band corresponding to the asymmetric stretching of Q_{Si}^4 (~1160 cm^{-1})[34] was not observed for BG_M in this work. The spectra between 800 and 1200 cm^{-1} were fitted with Gaussian functions, and integrated portions of the Q_{Si}^n ($n = 0$–3) groups are shown Figure 2B. The integrated portion of Q_{Si}^0 for BG_{Mg} was 2.4%, while those of BG_{Ca} and BG_{Sr} were 8.3 and 8.5%, respectively. The percentage of
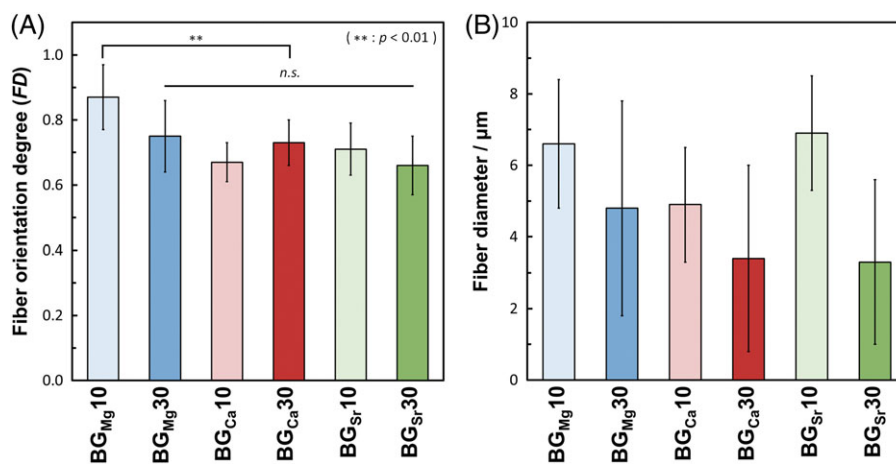
FIGURE 4. (A) Fiber orientation degree of BG_Mx, and (B) fiber diameter of BG_Mx. Error bars represent the standard deviation, and *n.s.* represent non-significant difference between the samples.

non-bridging oxygen (NBO) in the silicate groups of BG_M were calculated using the following equation:

$$NBO \ in \ Q_{Si}^n \ of \ BG_M(\%) = \frac{\sum_{n=0}^{3}\left\{(4-n) \times \left[Q_{Si}^n\right]_{BG_M}\right\}}{4 \times \sum_{n=0}^{3}\left[Q_{Si}^n\right]_{BG_M}} \times 100 \quad (4)$$

where n is number of bridging oxygen in Q_{Si}^n group, and $\left[Q_{Si}^n\right]_{BG_M}$ is integrated portions of the Q_{Si}^n groups in BG_M, which shown in Figure 2B. The values of BG_{Mg}, BG_{Ca}, and BG_{Sr} were 35.7%, 42.7%, and 44.0%, respectively. The NBO percentage indicates that the oxygen was in a SiO_4 tetrahedron, not connected to other SiO_4 tetrahedra.

Number-average molecular weights (M_n), weight-average molecular weights (M_w), and polydispersity indices (PDI, M_w/M_n) of PLLA and the composites are shown in Table I. The viscosities of the solutions for electrospinning are also shown in Table I, where the solutions were prepared with concentrations of 14 wt.% of PLLA in chloroform. The 10 vol.% BG_{Mg} composite was dissolved in chloroform at 10 wt.% of PLLA for electrospinning, with a viscosity of 1.4 Pa·s. The composites containing BG_{Mg} were found to have larger M_n values compared to those of the composites containing BG_{Ca} and BG_{Sr}. The composites containing 10 vol.% of glass powders had larger M_n values and solution viscosities, and smaller PDI values than those of the 30 vol.% samples.

Morphology of the fibermats

SEM images and fiber orientation angle histograms of the fibermats are shown in Figure 3. The fibers were aligned with the collector rotation direction (parallel to the yellow arrows), and the fiber orientation angles were distributed about a center of zero. The calculated *FD* values and diameters of the fibermats are shown in Figure 4. The *FD* of $BG_{Mg}10$ was significantly larger than the others ($p < 0.01$), whereas the *FD* values showed no significant differences between $BG_{Mg}30$, $BG_{Ca}x$, and $BG_{Sr}x$. The fiber

diameters of $BG_{Mg}10$, $BG_{Mg}30$, $BG_{Ca}10$, $BG_{Ca}30$, $BG_{Sr}10$, and $BG_{Sr}30$ were 6.6, 4.8, 4.9, 3.4, 6.9, and 3.3 μm, respectively. The diameters of the fibers containing 10 vol.% of BG_M were larger than those of 30 vol.% fibers. The *FD* and fiber diameter of the PLLA fibermat were 0.97 and 9.6 μm, respectively.

Ion-releasing behavior of the fibermats

Ion-releasing behaviors of BG_Mx in TBS are shown in Figure 5A–D. The released amount of Si, divalent (Mg^{2+}, Ca^{2+}, and Sr^{2+}), and Na^+ ions showed increasing trends with increased soaking time. The P ion releasing behaviors of the samples were significantly different. The amount of P ions released for $BG_{Mg}x$ increased to almost 100% with increased soaking time, whereas that of $BG_{Sr}10$ increased to approximately 65%, and those of $BG_{Ca}10$ and $BG_{Sr}30$ were approximately 30%, irrespectively the soaking time. Notably, the P ion releasing behavior of $BG_{Ca}30$ decreased to 0% with increased soaking time. The amounts of divalent ions released for $BG_{Ca}30$ and $BG_{Sr}30$ were smaller than those of the other BG_Mx. XRD patterns of BG_Mx after soaking in TBS for 9 days are shown in Figure 5E. $BG_{Ca}x$ and $BG_{Sr}x$ showed XRD peaks corresponding to $Ca_{10}(PO_4)_6(OH)_2$ (HA, ICCD card: 74–0566) and $Sr_5(PO_4)_3OH$ (Sr-HA, ICCD card: 33–1348), respectively. The XRD peak intensities of $BG_{Ca}30$ and $BG_{Sr}30$ were larger than those of $BG_{Ca}10$ and $BG_{Sr}10$, respectively.

Cell behavior on the fibermats

The cell numbers on BG_Mx are shown in Figure 6. $BG_{Mg}x$ showed significantly larger cell numbers than PLLA at all sampling times, and those of $BG_{Sr}x$ were significantly larger at 3 days. $BG_{Ca}10$ and $BG_{Ca}30$ showed significantly larger values than PLLA at 3rd and 1st day, respectively. Fluorescence images of the cells and cell orientation angle histograms are shown in Figure 7. The cells were aligned in the fiber oriented direction (i.e., the collector rotation direction), and the cell orientation angles were distributed about a center of zero. Calculated cell orientation degree (*CD*) values on
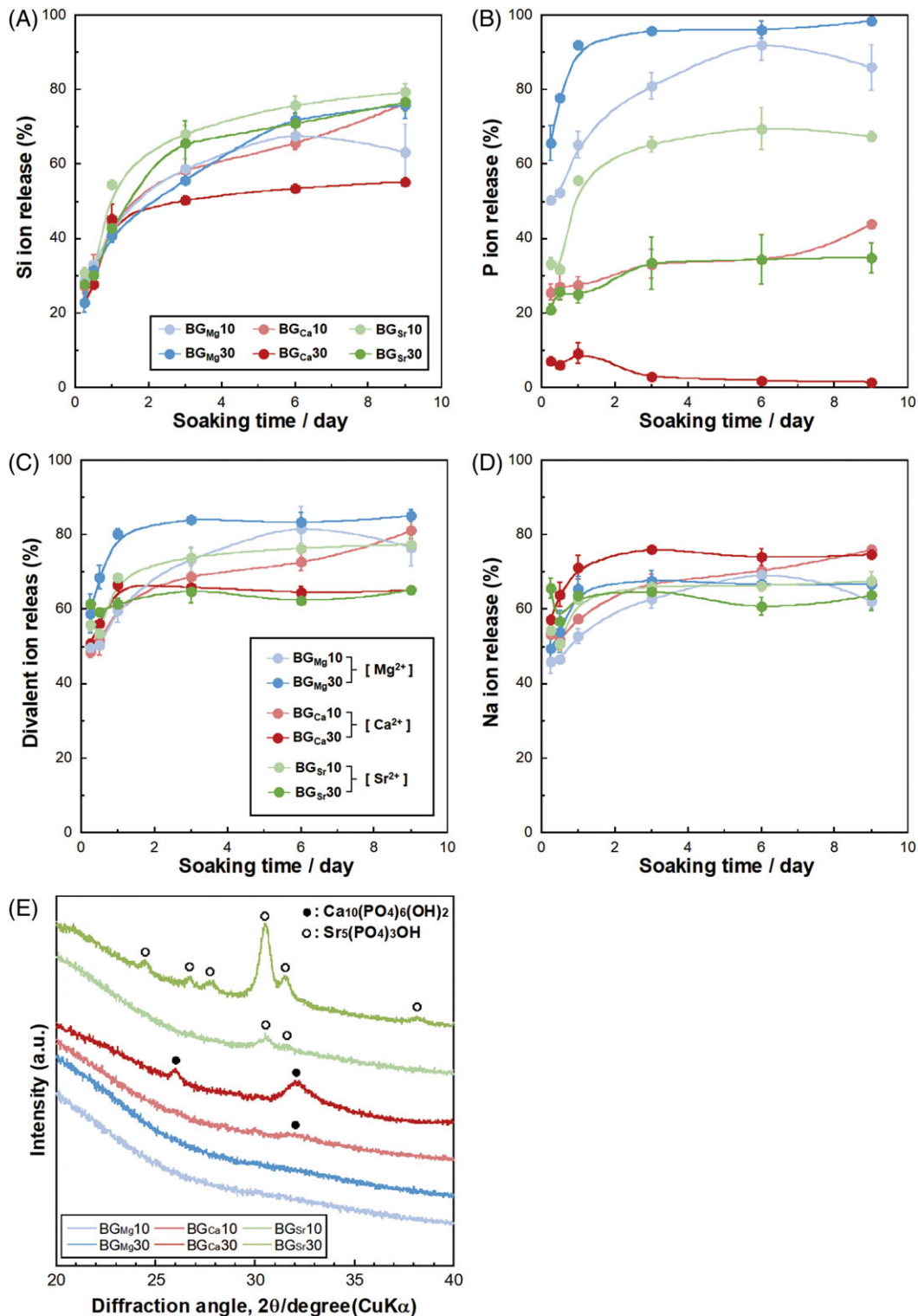
    BIOACTIVE GLASS/PLLAQ SCAFFOLDS TO CONTROL CELL ALIGNMENT AND PROLIFERATION

FIGURE 5. Percentages of the amount of released (A) Si, (B) P, (C) divalent (Mg, Ca, and Sr), and (D) Na ions in TBS from $BG_M x$. Error bars represent the standard deviation. (E) XRD patterns of $BG_M x$ after soaking in TBS for 9 days.

the fibermats are shown in Figure 8. The *CD* values of $BG_{Mg}10$, $BG_{Ca}10$, and $BG_{Sr}10$ were larger than those of $BG_{Mg}30$, $BG_{Ca}30$, and $BG_{Sr}30$, respectively: that is, the *CD* values of the fibers containing 10 vol.% of BG_M were larger than those of the 30 vol.% fibers.

DISCUSSION

The Raman band intensity of BG_{Mg} was smaller than those of BG_{Ca} and BG_{Sr}, which was also noted by Karakassides *et al.*[31] and Morikawa *et al.*[35] Raman bands corresponding to Q_{Si}^n and Q_p^0 were red-shifted (moved to lower frequencies) in
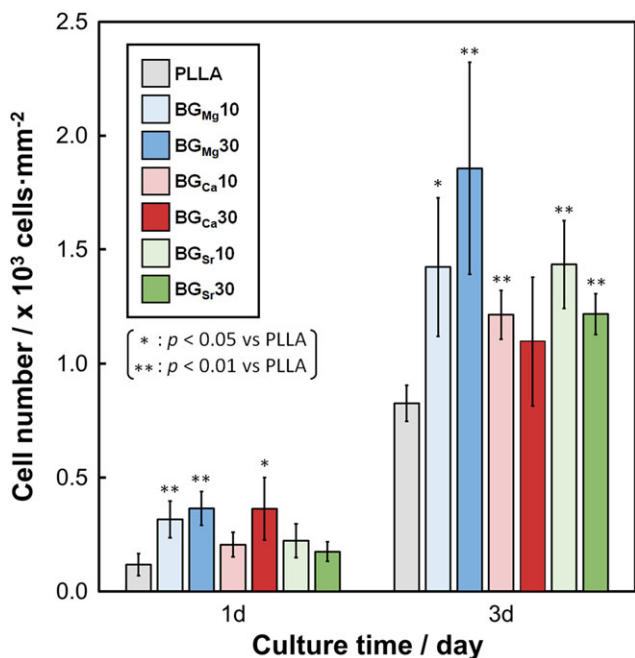
FIGURE 6. Cell numbers after 1–3 days on BG_Mx. Error bars represent the standard deviation.

the order: BG_{Mg}, BG_{Ca}, and BG_{Sr}. This can be explained by the field strength. Dietzel suggested that the field strength (F), which is the simplified Coulomb's force of the ions in glass, is defined as follows[36,37]:

$$F = \frac{Z_c}{d^2} \left(valance/\text{Å}^2 \right) \qquad (4)$$

where Z_c is the ionic charge and d is the interatomic distance between the cation and oxygen. The F values of Mg, Ca, and Sr were 0.53 or 0.46 (four-fold or six-fold coordination), 0.33, and 0.28, respectively.[36] The bonding strength decreased in the order Mg-O, Ca-O, and Sr-O, causing the observed differences in the silicate and phosphate stretching vibration frequencies.[31,35] The NBO contents in BG_{Mg} was larger than BG_{Ca}, and BG_{Sr}. According to Dietzel, Mg can be classified by the intermediates, which can switch role network modifier and former.[36,37] Watts *et al.* reported that Mg can enter a silicate network as MgO_4 tetrahedral units, which can act as a network former.[38] Thus, Mg in BG_{Mg} acts as a network former to enter the silicate network; which means that Mg is less effective at breaking the silicate chains than Ca and Sr. Consequently, BG_{Mg} showed a smaller NBO content than those of BG_{Ca} and BG_{Sr}.

The M_n of the composite pellets decreased from that of PLLA, since absorbed water in the glass powder break the PLLA polymer chain during the melt-blending process. The absorbed water in the glass powder was bonded to the NBO in the glass structure. Accordingly, BG_{Mg} contained less absorbed water than BG_{Ca} and BG_{Sr} did, since the NBO content of BG_{Mg} was less than that of the others. Thus, the M_n of the composite containing BG_{Mg} was larger than those of BG_{Ca} and BG_{Sr}. Similarly, the composites containing 10 vol.%

of the glass powder had larger M_n values than those of the 30 vol.% composites, because they contained less glass powder (i.e., containing less amount of NBO). Generally, when a polymer with a larger M_n is dissolved in a solvent, its viscosity will be higher than a solution of the same polymer with a smaller M_n.[39] Correspondingly, the viscosity of the solutions had larger values for BG_{Mg} composites than those of the BG_{Ca} and BG_{Sr} solutions. Also, the composites containing 10 vol.% of the glass powder showed larger viscosities than the 30 vol.% composites.

In electrospinning, polymer fibers are formed by the creation and elongation of an electrified fluid jet.[40] The velocities of the jets measured using a high framerate video camera were in the range from 0.5 to 5 m·s^{-1}.[40] A collector speed of 4.7 m·s^{-1} was used in this work; accordingly, the fibers could be collected while elongating in the collector rotation direction. If the solution formed a stable jet during the electrospinning conditions, the resulting fibers showed oriented morphologies. The composites containing 10 vol.% of BG_M formed stable jets during electrospinning, whereas the 30 vol.% composites formed branched fluid jets. Generally, jet instability induces a branched fluid jet;[39] the composites with 30 vol.% BG_M formed unstable jets more easily than the 10 vol.% composites due to their larger PDI values and because they contained larger amounts of glass powder. Branched fluid jets can be induced by the random angle distribution of the fibers, since there is an angular difference from the primary jet. This may also lead to larger FD values for the fibermats containing 10 vol.% of BG_M than those of the 30 vol.% composites. A branched jet forms by ejecting smaller jets from the surface of the primary jets, which have smaller diameters than the primary jet.[39] Thus, $BG_{Mg}30$, $BG_{Ca}30$, and $BG_{Sr}30$ had smaller fiber diameters and larger FD values than those of $BG_{Mg}10$, $BG_{Ca}10$, and $BG_{Sr}10$, respectively.

The released amounts of divalent and P ions from $BG_{Ca}x$ and $BG_{Sr}x$ were smaller than that of $BG_{Mg}x$, owing to precipitation of HA and Sr-HA, respectively. No XRD peaks were observed for $BG_{Mg}x$, since the Mg^{2+} ions inhibited the precipitation of apatite.[41] The released amounts of Si ions from $BG_{Ca}30$ and $BG_{Sr}30$ were smaller than those of the others, due to formation of an Si-OH gel layer,[42–44] which induced apatite formation.[45] The released amounts of P and divalent ions from $BG_{Ca}30$ and $BG_{Sr}30$ were smaller than those of $BG_{Ca}10$ and $BG_{Sr}10$, respectively. That is, large amount of the ions from $BG_{Ca}30$ and $BG_{Sr}30$ were used for precipitation of HA and Sr-HA than those of $BG_{Ca}10$ and $BG_{Sr}10$, respectively. Thus, XRD intensities of $BG_{Ca}30$ and $BG_{Sr}30$ were larger than those of $BG_{Ca}10$ and $BG_{Sr}10$, respectively. $BG_{Mg}x$ showed similar/larger Si release percentage compare with the others, since Si-O-Mg bonds weaken the glass network structure and the resistance to hydrolysis[38,46,47] despite lower NBO content in BG_{Mg}. The released amounts of divalent (i.e., Mg^{2+}, Ca^{2+}, and Sr^{2+}) and Si ions from the fibermats increased with increased soaking time, which is expected to improve bone regeneration.

The cell numbers of $BG_{Mg}x$ were significantly larger than those of the control after 1 and 3 days of culturing. This was caused by the dissolved Mg^{2+} ions from the $BG_{Mg}x$, which improved cell adhesion and proliferation.[12–15] $BG_{Sr}x$ showed
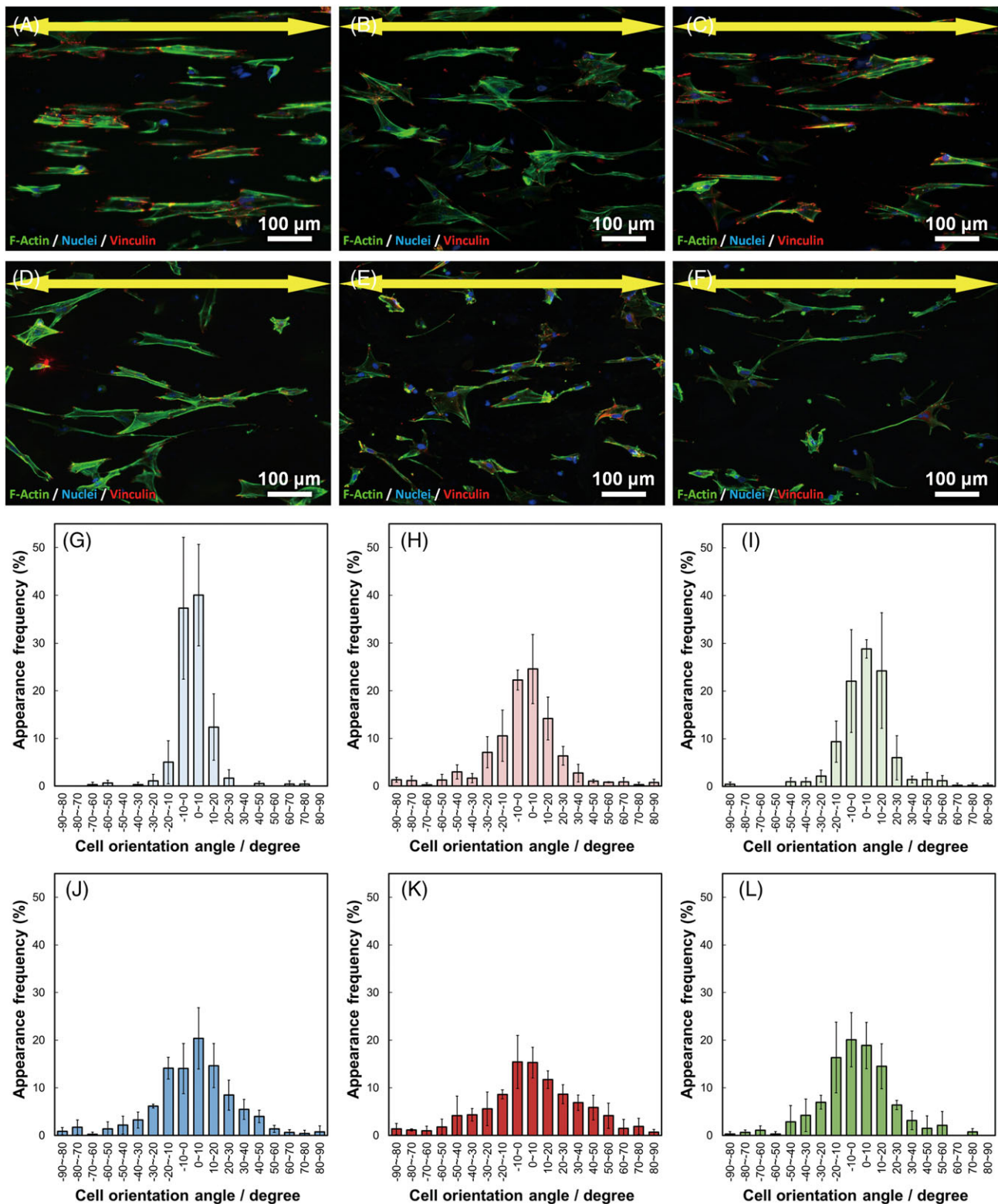
FIGURE 7. Fluorescence images of osteoblasts cultured on (A) $BG_{Mg}10$, (B) $BG_{Ca}10$, (C) $BG_{Sr}10$, (D) $BG_{Mg}30$, (E) $BG_{Ca}30$, and (F) $BG_{Sr}30$. Arrows indicate the collector rotation direction. Green: F-actin, blue: nuclei, and red: vinculin. Cell orientation angle histograms for (G) $BG_{Mg}10$, (H) $BG_{Ca}10$, (I) $BG_{Sr}10$, (J) $BG_{Mg}30$, (K) $BG_{Ca}30$, and (L) $BG_{Sr}30$. Error bars represent the standard deviation.

a significantly larger cell number after 3 days of culturing compared to that of the control, since the dissolved Sr^{2+} ions from $BG_{Sr}x$ improved proliferation.

In our previous report, primary osteoblasts on oriented collagen substrate were aligned parallel to the collagen fiber orientation.[6] Cell produced collagen matrix oriented in the
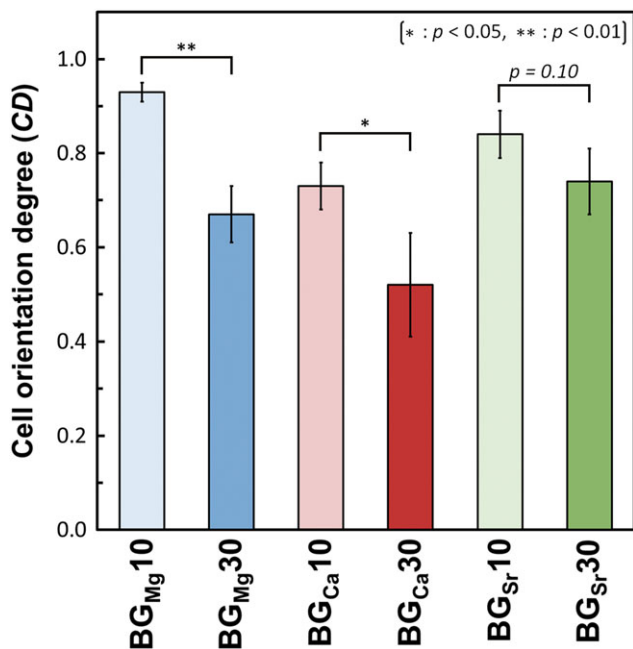
FIGURE 8. Cell orientation degree of $BG_M x$. Error bars represent the standard deviation.

direction of cellular elongation, and the *c*-axis of deposited apatite crystals showed preferential alignment along the direction of the newly synthesized collagen fibers[6]. Thus, control of the osteoblast alignment can construct the bone tissue anisotropy depending on the alignment of the cells themselves: that is, strongly oriented osteoblasts can produce the anisotropic bone tissues. Sun *et al.* reported that the cells adhered to a single fiber when the diameter of fiber was larger than 10 μm, whereas the cells adhered to several fibers and spread when the diameter of the fibers was <10 μm.[48] In this study, the osteoblasts adhered on the fabricated microfibermats elongate their stress fiber along the fibermats, because the dynamics of actin organization is strictly regulated by the spatial geometry involving the scaffold curvature.[49] In microfibermats, the fiber diameter with >10 μm could helpful to improve cell alignment by inhibiting cells spread between fibers.[48] That is, the orientation degree of cells adhered to a single fiber can be easily controlled by controlling the morphology of the fibermats. $BG_{Mg}10$, $BG_{Ca}10$, and $BG_{Sr}10$ showed larger *CD* values than those of $BG_{Mg}30$, $BG_{Ca}30$, and $BG_{Sr}30$, respectively, since the fiber diameters of the 10 vol% BG_M fibermats were larger than those of the 30 vol.% fibermats. Notably, the cells on $BG_{Mg}10$ and $BG_{Sr}10$, whose fiber diameters were larger than 6 μm, adhered to some single fibers, resulting in *CD* values that were larger than those of the other samples. These results indicate that we can manipulate the cell orientation and proliferation freely by controlling the fiber diameter and the ionic species released from the bioactive glasses.

CONCLUSION

A novel bifunctional biomaterial, which can control osteoblast orientation as well as cell proliferation, was established. The oriented $BG_M x$/PLLA composite fibermats enabled cell alignment along the fibers and promoted cell proliferation due to the released ions from the bioactive glasses. The degree of fiber orientation was successfully controlled by modulating the content of the bioactive glasses and fiber diameters. The cell proliferation was significantly upregulated by the release of Mg^{2+} and Sr^{2+} ions from the bioactive glasses. The cell orientation was determined by the cell recognition of the fiber orientation and adherence along single fibers or the formation of cell branches protruding across multiple fibers. The obtained results not only indicated that the fabricated composites could control the cytoskeletal arrangement of osteoblasts along the fiber direction, but also, the controlled release of ions successfully improved osteoblast proliferation. These findings can lead to the development of innovative multifunctional biomaterials suitable for tissue regeneration treatments by the optimization of the structural properties of the scaffolds and inorganic ion element release.

REFERENCES

1. Weiner S, Wagner HD. The material bone: Structure-mechanical function relations. Annu Rev Mater Sci 1998;28:271–298.
2. Seto J, Gupta HS, Zaslansky P, Wagner HD, Fratzl P. Tough lessons from bone: Extreme mechanical anisotropy at the mesoscale. Adv Funct Mater 2008;18:1905–1911.
3. Nakano T, Kaibara K, Tabata Y, Nagata N, Enomoto S, Marukawa E, Umakoshi Y. Unique alignment and texture of biological apatite crystallites in typical calcified tissues analyzed by microbeam x-ray diffractometer system. Bone 2002;31:479–487.
4. Ishimoto T, Nakano T, Umakoshi Y, Yamamoto M, Tabata Y. Degree of biological apatite *c*-axis orientation rather than bone mineral density controls mechanical function in bone regenerated using recombinant bone morphogenetic protein-2. J Bone Miner Res 2013;28:1170–1179.
5. Matsugaki A, Aramoto G, Ninomiya T, Sawada H, Hata S, Nakano T. Abnormal arrangement of a collagen/apatite extracellular matrix orthogonal to osteoblast alignment is constructed by a nanoscale periodic surface structure. Biomaterials 2015;37:134–143.
6. Matsugaki A, Isobe Y, Saku T, Nakano T. Quantitative regulation of bone-mimetic, oriented collagen/apatite matrix structure depends on the degree of osteoblast alignment on oriented collagen substrates. J Biomed Mater Res A 2015;103:489–499.
7. Hench LL. The story of Bioglass®. J Mater Sci Mater Med 2006;17:967–978.
8. Hench LL, Polak JM. Third-generation biomedical materials. Science 2002;295:1014–1017.
9. Xynos ID, Edgar AJ, Buttery LDK, Hench LL, Polak JM. Ionic products of bioactive glass dissolution increase proliferation of human osteoblasts and induce insulin-like growth factor II mRNA expression and protein synthesis. Biochem Biophys Res Commun 2000;276:461–465.
10. Xynos ID, Edgar AJ, Buttery LDK, Hench LL, Polak JM. Gene-expression profiling of human osteoblasts following treatment with the ionic products of Bioglass® 45S5 dissolution. J Biomed Mater Res 2001;55:151–157.
11. Xynos ID, Hukkanen JMV, Batten JJ, Buttery DL, Hench LL, Polak MJ. Bioglass®45S5 stimulates osteoblast turnover and enhances bone formation in vitro: Implications and applications for bone tissue engineering. Calcif Tissue Int 2000;67:321–329.
12. Takeichi M, Okada TS. Roles of magnesium and calcium ions in cell-to-substrate adhesion. Exp Cell Res 1972;74:51–60.

BIOACTIVE GLASS/PLLAQ SCAFFOLDS TO CONTROL CELL ALIGNMENT AND PROLIFERATION

13. Zreiqat H, Howlett CR, Zannettino A, Evans P, Schulze-Tanzil G, Knabe C, Shakibaei M. Mechanisms of magnesium-stimulated adhesion of osteoblastic cells to commonly used orthopaedic implants. J Biomed Mater Res 2002;62:175–184.

14. Wolf FI, Cittadini A. Magnesium in cell proliferation and differentiation. Front Biosci 1999;4:D607–D617.

15. Yamada S, Ota Y, Obata A, Kasuga T. Osteoblast-like cell responses to ion products released from magnesium- and silicate-containing calcium carbonates. Biomed Mater Eng 2017;28:47–56.

16. Chattopadhyay N, Quinn SJ, Kifor O, Ye C, Brown EM. The calcium-sensing receptor (CaR) is involved in strontium ranelate-induced osteoblast proliferation. Biochem Pharmacol 2007;74:438–447.

17. Marie PJ. Strontium ranelate: A physiological approach for optimizing bone formation and resorption. Bone 2006;38:10–14.

18. Marie PJ. Strontium ranelate: New insights into its dual mode of action. Bone 2007;40:S5–S8.

19. Marie PJ. The calcium-sensing receptor in bone cells: A potential therapeutic target in osteoporosis. Bone 2010;46:571–576.

20. Barbara A, Delannoy P, Denis BG, Marie PJ. Normal matrix mineralization induced by strontium ranelate in MC3T3-E1 osteogenic cells. Metabolism 2004;53:532–537.

21. Obata A, Hotta T, Wakita T, Ota Y, Kasuga T. Electrospun microfiber meshes of silicon-doped vaterite/poly(lactic acid) hybrid for guided bone regeneration. Acta Biomater 2010;6:1248–1257.

22. Fee T, Surianarayanan S, Downs C, Zhou Y, Berry J. Nanofiber alignment regulates NIH3T3 cell orientation and cytoskeletal gene expression on electrospun PCL+gelatin nanofibers. PLoS One 2016;11:e0154806.

23. Madhurakkat Perikamana SK, Lee J, Ahmad T, Jeong Y, Kim D-G, Kim K, Shin H. Effects of immobilized BMP-2 and nanofiber morphology on in vitro osteogenic differentiation of hMSCs and in vivo collagen assembly of regenerated bone. ACS Appl Mater Interfaces 2015;7:8798–8808.

24. Lee J-h, Lee YJ, H-j C, Shin H. Guidance of in vitro migration of human mesenchymal stem cells and in vivo guided bone regeneration using aligned electrospun fibers. Tissue Eng Part A 2013;20:2031–2042.

25. Tujunen N-M, Fujikura K, Obata A, Kasuga T. Aligned electrospun siloxane-doped vaterite/poly(l-lactide) composite fibremats: Evaluation of their tensile strength and cell compatibility. J Biomater Sci Polym Ed 2013;24:2096–2109.

26. Matsugaki A, Fujiwara N, Nakano T. Continuous cyclic stretch induces osteoblast alignment and formation of anisotropic collagen fiber matrix. Acta Biomater 2013;9:7227–7235.

27. Wong G, Cohn DV. Separation of parathyroid hormone and calcitonin-sensitive cells from non-responsive bone cells. Nature 1974;252:713–715.

28. Umeno A, Kotani H, Iwasaka M, Ueno S. Quantification of adherent cell orientation and morphology under strong magnetic fields. IEEE Trans Magn 2001;37:2909–2911.

29. Mysen BO, Virgo D, Scarfe CM. Relations between the anionic structure and viscosity of silicate melts—A Raman-spectroscopic study. Am Mineral 1980;65:690–710.

30. Sun Y, Zhang Z, Liu L, Wang X. FTIR, Raman and NMR investigation of $CaO-SiO_2-P_2O_5$ and $CaO-SiO_2-TiO_2-P_2O_5$ glasses. J Non Cryst Solids 2015;420:26–33.

31. Karakassides MA, Saranti A, Koutselas I. Preparation and structural study of binary phosphate glasses with high calcium and/or magnesium content. J Non Cryst Solids 2004;347:69–79.

32. Lee S, Maeda H, Obata A, Ueda K, Narushima T, Kasuga T. Structures and dissolution behaviors of $MgO-CaO-P_2O_5-Nb_2O_5$ glasses. J Non Cryst Solids 2016;438:18–25.

33. Pedone A, Malavasi G, Menziani MC. Computational insight into the effect of CaO/MgO substitution on the structural properties of Phospho-silicate bioactive glasses. J Phys Chem C 2009;113:15723–15730.

34. Lin C-C, Chen S-F, Leung KS, Shen P. Effects of CaO/P_2O_5 ratio on the structure and elastic properties of $SiO_2-CaO-Na_2O-P_2O_5$ bioglasses. J Mater Sci Mater Med 2012;23:245–258.

35. Morikawa H, Lee S, Kasuga T, Brauer DS. Effects of magnesium for calcium substitution in $P_2O_5-CaO-TiO_2$ glasses. J Non Cryst Solids 2013;380:53–59.

36. Varshneya AK. Chapter 3—glass formation principles. Fundamentals of Inorganic Glasses. San Diego, CA: Academic Press; 1994. p 27–59.

37. Dietzel A. Die Kationenfeldstärken und ihre Beziehungen zu Entglasungsvorgängen, zur Verbindungsbildung und zu den Schmelzpunkten von Silicaten. Ztschr Elektrochem 1942;48:9–23.

38. Watts SJ, Hill RG, O'Donnell MD, Law RV. Influence of magnesia on the structure and properties of bioactive glasses. J Non Cryst Solids 2010;356:517–524.

39. Seeram R, Kazutoshi F, Wee-Eong T, Teik-Cheng L, Zuwei M. Electrospinning Process. An Introduction to Electrospinning and Nanofibers. Singapore: World Scientific Publishing; 2012. p 90–154.

40. Reneker DH, Yarin AL. Electrospinning jets and polymer nanofibers. Polymer 2008;49:2387–2425.

41. Salimi MH, Heughebaert JC, Nancollas GH. Crystal growth of calcium phosphates in the presence of magnesium ions. Langmuir 1985;1:119–122.

42. Hench LL, Splinter RJ, Allen WC, Greenlee TK. Bonding mechanisms at the interface of ceramic prosthetic materials. J Biomed Mater Res 1971;5:117–141.

43. Maçon ALB, Lee S, Poologasundarampillai G, Kasuga T, Jones JR. Synthesis and dissolution behaviour of CaO/SrO-containing sol–gel-derived 58S glasses. J Mater Sci 2017;52:8858–8870.

44. Filgueiras MR, La Torre G, Hench LL. Solution effects on the surface reactions of a bioactive glass. J Biomed Mater Res 1993;27:445–453.

45. Kokubo T, Takadama H. How useful is SBF in predicting in vivo bone bioactivity? Biomaterials 2006;27:2907–2915.

46. Brauer DS, Karpukhina N, Kedia G, Bhat A, Law RV, Radecka I, Hill RG. Bactericidal strontium-releasing injectable bone cements based on bioactive glasses. J R Soc Interface 2012;10:20120647.

47. Lee S, Nakano T, Kasuga T. Formation and structural analysis of $15MgO-15CaO-8P_2O_5-4SiO_2$ glass. J Non Cryst Solids 2017;457:73–76.

48. Sun T, Norton D, McKean RJ, Haycock JW, Ryan AJ, MacNeil S. Development of a 3D cell culture system for investigating cell interactions with electrospun fibers. Biotechnol Bioeng 2007;97:1318–1328.

49. Dunn GA, Heath JP. A new hypothesis of contact guidance in tissue cells. Exp Cell Res 1976;101:1–14.